Diffusive homeostasis in a self-organizing recurrent neural network: local neuron density predicts firing rates

Fabian Schubert[1,2�*], Daniel Miner[1,3‡], Jochen Triesch[1†],

1 Frankfurt Institute for Advanced Studies, Frankfurt am Main, Germany
2 Goethe University Frankfurt, Institute for Theoretical Physics, Frankfurt am Main, Germany
3 University of Göttingen, Third Institute of Physics, Göttingen, Germany

☢This author performed parts of the programming, analysis and writing and contributed to the conceptualization. Most of the author's work was carried out as a member of **1**.
‡This author performed parts of the programming, provided significant expertise and consultation and contributed to the conceptualization. Most of the author's work was carried out as a member of **1**.
†This author provided significant expertise and consultation and contributed to the conceptualization.
* E-mail: fschubert@fias.uni-frankfurt.de

Abstract

Firing rates of cortical neurons are very heterogeneous, approximately following a log-normal distribution. A similar log-normal like distribution also describes the efficacies of synapses connecting these neurons. Additionally, there is experimental evidence for an over-representation of bidirectional synaptic connectivity and power-law life-times of newly created synapses. It is presently unclear how all these features of cortical activity and wiring come about. Here we present a new spiking neural network model to explain these findings. The model is a member of the family of self-organizing recurrent neural network models with leaky integrate-and-fire neurons (LIF-SORN) and explains the above phenomena through the interaction of different plasticity mechanisms shaping network structure and dynamics. In particular, it incorporates a recently proposed mechanism for firing rate homeostasis based on the diffusion of nitric oxide. This mechanism supports a heavy-tailed, log-normal like distribution of firing rates. Interestingly, we find that the spatial configuration of neurons in the model determines individual homeostatic firing rate targets in the network. To understand this effect, we develop a theory to analytically describe the relationship between firing rates and local neuron density. The theory predicts that high firing rates are associated with low neuron density. We find partial support for this prediction by reanalyzing recent calcium imaging data.

Author summary

Neurons in the neocortex have a very broad distribution of firing rates such that most neurons fire very little while a few are highly active. Similarly, the distribution of the strengths of synapses connecting these neurons is also very broad. How these and other features of cortical networks arise is currently unknown. Here we present a model that explains a whole range of such phenomena as a consequence of network self-organization driven by the interaction of a few plasticity mechanisms. Furthermore, the model makes the novel prediction that a diffusive mechanism stabilizing the network's firing rates induces a systematic relationship between a neuron's average activity and the density of neurons in its vicinity.

Introduction

The statistical distributions of both neuronal firing rates and synaptic efficacies in cortex are highly skewed and approximately log-normal [1, 2]. This heterogeneity is thought to be involved in the preservation of stable synaptic structures while still allowing synaptic rewiring in the context of learning [3, 4]. Furthermore, a broad distribution of firing rates may serve to improve encoding of external stimuli [5]. Although the functional role of these statistical features have been investigated, the fundamental mechanisms required to give rise to these properties are still a point of debate. Combinations of additive STDP and multiplicative dynamics have been proposed as well as modified, weight dependent STDP rules in order to explain the heavy-tailed distribution of synaptic weights [6, 7].

Neuronal activity is affected by homeostatic mechanisms that regulate firing rates on different timescales. Experimental studies have shown that populations of neurons not only exhibit broad distributions of firing rates, but also that these distributions are maintained on a single-cell level by means of individual homeostatic targets of activity [8, 9]. However, the biological origin of these intercellular differences in target activity are still unknown.

Recently, Sweeney et al. have introduced a model of diffusive homeostasis [10], suggesting that diffusive signaling via nitric oxide (NO) could serve as an explanation for the broad, heavy-tailed firing rate distribution, while stabilizing the overall population firing rate. Through the diffusive signal, each neuron receives an estimate of the local network activity. The diffusive homeostasis aims to keep this at a constant level, while allowing individual neurons to have firing rates that differ strongly from the mean.

Here we present a spiking neural network model that combines this diffusive homeostasis mechanism with other plasticity mechanisms to reproduce a range of structural and dynamic features of cortical wiring. The model is a member of the family of self-organizing recurrent neural network models with leaky integrate-and-fire neurons (LIF-SORN). It gives rise to log-normal like distributions of firing rates and synaptic efficacies as observed experimentally. Furthermore, it reproduces an over-representation of bidirectional connections and power-law life-times of newly created synaptic connections. As an additional feature of network topology, the heterogeneity of excitatory firing rates allows for the emergence of strongly influential neurons, characterized by highly above-average mean outgoing synaptic weights. Importantly, the model leads to different firing rate targets for individual neurons based on their spatial configuration, such that high firing rates are associated with low neuron density. We then develop a mathematical theory to describe this effect analytically.

Table 1. Parameters of synaptic connections.

parameter	EE	IE	EI	II
connection fraction	$\to 0.1$	0.1	0.1	0.5
initial connection strength	$0.0001\,\mathrm{mV}$	$1.5\,\mathrm{mV}$	$-1.5\,\mathrm{mV}$	$-1.5\,\mathrm{mV}$
conduction delay	$1.5\,\mathrm{ms}$	$0.5\,\mathrm{ms}$	$1.0\,\mathrm{ms}$	$1.0\,\mathrm{ms}$

Table 2. Parameters of LIF neuron.

parameter	exc. neur.	inh. neur.
E_l	-60 mV	-60 mV
τ_m	20 ms	20 ms
V_r	-70 mV	-60 mV
σ	$\sqrt{5}$ mV	$\sqrt{5}$ mV
V_t	dynamic, subject to Intrinsic Plasticity	-58 mV

Materials and methods

Network simulation

Our model consists of a two-dimensional layer of 400 excitatory and 80 inhibitory leaky integrate and fire (LIF) model neurons. The neurons were assigned random positions across a square area of $1000\,\mu\mathrm{m} \times 1000\,\mu\mathrm{m}$. The connection probability between two neurons was calculated from a distance dependent Gaussian function with a standard deviation of $200\,\mu\mathrm{m}$. All synapses were simulated with a fixed (distance independent) conduction delay. Recurrent connections were absent at the beginning and then generated at a certain rate throughout the whole simulation, see section on synaptic plasticity. All other connections (EI,IE and II) were added before starting the simulation until a desired connection fraction was reached. For excitatory to inhibitory (IE) and inhibitory to excitatory (EI) synapses, the connection fraction was set to 0.1, and 0.5 for recurrent inhibitory synapses (II). These connections were kept at a fixed connection strength throughout the simulation. Where possible, parameters were set to the same values as in previous versions of the LIF-SORN [11], where they were chosen to approximate L5 data. In contrast to previous versions, the inhibitory threshold was kept at a fixed value which was tuned to provide stable inhibitory background activity. Recurrent excitatory synapses were subject to a number of plasticity mechanisms.

Neuron model

We used a leaky integrate-and-fire-model with a simple additive synaptic transmission model for all neurons in the network, whose dynamics are described by a stochastic differential equation:

$$\tau_m dV_i = -\left(V_i - E_l\right)dt + \sqrt{\tau_m}\sigma dW_i + \tau_m \sum_{j,k} w_{ij}^{\mathrm{effective}}\delta\left(t_{\mathrm{spike},j}^k + t_{\mathrm{delay}} - t\right) \quad (1)$$

where V is the membrane potential, E_l is the equilibrium membrane potential, τ_m is the membrane time constant, σ is the standard deviation of the noise term and dW is the standard Wiener process. A neuron generates a spike when its membrane potential reaches the threshold voltage V_t. The voltage is then reset to V_r. A refractory period was not implemented. A presynaptic spike causes a simple (delayed, see Table 1) increment of the membrane potential of the postsynaptic neuron by $w_{ji}^{\mathrm{effective}}$. Table 2 summarizes the aforementioned set of parameters.

Synaptic plasticity

Synapse Generation: New excitatory-to-excitatory synapses were generated at an average rate of 920 per second. For efficiency, this was implemented by drawing an integer number from a normal distribution with mean 920 and standard deviation $\sqrt{920}$ once per second and simultaneously inserting this number of synapses. This growth rate was tuned to achieve the desired target connection fraction of 0.1 (see Table 1). Just as for the connections created before the simulation started, the connection probability between excitatory neurons was proportional to a distance-dependent Gaussian with the same width.

The synapse insertion rate allowed good control over the long-term connection fraction since the latter exhibited a proportional dependence on the growth rate. Moreover, we ran multiple versions of the network using the same synapse generation rate, but switching between distance-dependent/uniform connection probabilities and diffusive/non-diffusive homeostasis to see how sensitive the resulting connection fraction was with respect to these changes. It turned out that diffusive vs. non-diffusive homeostasis was practically indistinguishable in terms of the resulting connection fraction and distance-dependent vs. uniform connection probabilities differed only marginally ($\approx 5\%$ increase in connection fraction for uniform connection probabilities).

Synaptic Pruning: The process of synaptic pruning was similarly carried out by checking for EE synapses below a threshold of 10^{-6} mV once each second (same instant as growth) and removing them simultaneously, and thus adding them again to the set of "potential" connections from which the growth process draws new connections.

Spike Timing Dependent Plasticity: An additive STDP rule was used as described, e.g., in [12]. The change of weight between two neurons due to a pre- and postsynaptic spike ($i \rightarrow j$) is defined as:

$$\Delta w_{ji} = \sum_{k} \sum_{l} W(t_j^l - t_i^k) \tag{2}$$

$$W(\Delta t) = \begin{cases} A_+ \exp(-\Delta t / \tau_+), & \Delta t \geq 0 \\ A_- \exp(\Delta t / \tau_-), & \Delta t < 0 \,. \end{cases} \tag{3}$$

Indexes k and l refer to the k-th and l-th pre- and postsynaptic spike respectively. Parameters were chosen to approximate data from [13] and [14], namely $\tau_+ = 15$ ms, $A_+ = 15$ mV, $\tau_- = 30$ ms and $A_- = -7.5$ mV. This choice of parameters gives a zero integral for the STDP window and ensured that uncorrelated pre- and postsynaptic spiking activity will exhibit a balance between weight potentiation and depression. We used the "nearest neighbor" approximation for the sake of reduction of computational effort, only calculating the effect of the most recent pre-post pair of spikes for potentiation and post-pre pair for depression, yielding roughly the same value as the full summation due to the fast decay times τ_+ and τ_- of the STDP-window and the low average firing rates in the network [15].

Synaptic Normalization: For the same reasons of efficiency, synaptic normalization was applied at the same rate as synaptic growth/pruning, updating each w_{ji} from neuron i to neuron j as follows:

$$w_{ji} \rightarrow w_{ji} \frac{w_{\text{total}}}{\sum_i w_{ji}} \,. \tag{4}$$

w_{total} was set to different values for each of the four types of connections between the excitatory and inhibitory pools of neurons. Except for the dynamically populated EE-synapses these values were determined by multiplying the average synaptic efficacy for this connection type from Table 1 with the average number of connections of this type projecting to a neuron. This yielded $w_{\text{total,IE}} = 60$ mV, $w_{\text{total,EI}} = -12$ mV,

$w_{\text{total,II}} = -60\,\text{mV}$. $w_{\text{total,EE}}$ was set to $40\,\text{mV}$, corresponding to a mean synaptic weight of $1\,\text{mV}$, given a targeted EE-connection fraction of 0.1 and a population of 400 excitatory neurons.

Synaptic normalization can be regarded as a form of homeostatic control of activity in the sense that it prevents neurons from receiving an excess of excitatory input due to large synaptic weights. However, it is agnostic with respect to the actual output activity, which is also influenced by the presynaptic firing activity, and therefore does not conflict with a potentially broad distribution of firing rates.

Short Term Plasticity: A short term plasticity (STP) mechanism acting on recurrent excitatory connections was implemented as presented in [16] as an additional stabilization of network activity. As also stated in [11], including STP reduced the need for precise parameter tuning to achieve stable network activity. It modulates the effective synaptic weights by multiplying the value stored in the weight matrix w_{ji} by two dynamic variables x and u, $w^{\text{effective}} = w \cdot x \cdot u$, each synapse owning a pair (x, u). The dynamics of these variables are given by:

$$\dot{x} = \frac{1-x}{\tau_d}, \ \dot{u} = \frac{U-u}{\tau_f} \tag{5}$$

where τ_d and τ_f are the time constants of depression and facilitation, respectively. Each presynaptic spike furthermore causes a change of x and u by

$$x \to x - xu, \ u \to u + U(1-u) \,. \tag{6}$$

We chose $U = 0.04$, $\tau_d = 0.5\,\text{s}$ and $\tau_f = 2\,\text{s}$ as a rough approximation of the values that were experimentally observed [16]. As an aside, for our choice of variables, a Poisson input with a constant rate would achieve the best synaptic transmission at a rate of $\sim 4.5\,\text{Hz}$, corresponding to $xu \approx 0.2$.

Intrinsic plasticity

Apart from dynamic processes within synapses which contribute to a stabilization of the network's activity, neurons possess internal mechanisms capable of maintaining a desired regime of activity. Regular-spiking cells are known to down-(up-)regulate their firing rate upon increased (decreased) input on a timescale of tens of milliseconds [17, 18]. The network itself was not expected to exhibit fast changes of synaptic input since our simulation did not incorporate any rapidly changing external drive, which allowed us to neglect this feature. On the other hand, a similar form of adaptation as a reaction to reduced or increased input can be observed on a timescale of hours to days [19]. In the latter case, a long-term change in excitability can be attributed to an altered number of ionic channels. This contrasts the former short-term adaptation, which happens due to the depletion of certain ionic currents in the cell, acting on slower timescales than the fast spike initiation dynamics in the cell, but altering their firing rate. A simple form of intrinsic homeostasis was implemented in the original LIF-SORN by altering the neurons' firing threshold based on the deviation from a target firing rate. Here, we implemented a new model of slow intrinsic homeostasis, based on the work in [10]. In the following, we describe both models in detail.

Our original model of homeostatic control was described by the following differential equation:

$$\dot{V}_t = \eta_{\text{IP}}(r - r_{\text{IP}}) \tag{7}$$

with r as the neuron's firing rate and r_{IP} the target firing rate, η_{IP} the rate of threshold adaptation and r the estimated firing rate of a single excitatory neuron. In practice, this was implemented in discrete steps , estimating the firing rate by $r = N_{\text{spikes}}/\Delta t$,

Table 3. Parameters of homeostatic intrinsic plasticity.

parameter	value
r_{IP}	$3\,Hz$
η_{IP}	$0.1\,mV$
$[Ca^{2+}]_{spike}$	1
$\tau_{Ca^{2+}}$	$10\,ms$
τ_{nNOS}	$100\,ms$
D	default: $10\,\mu m^2 ms^{-1}$
λ	$0.1\,s^{-1}$
τ_{V_t}	$2500\,s$

with N_{spikes} as the number of spikes within each interval. We replaced this mechanism by a a diffusive homeostatic model by Sweeney et al. that consists of a set of differential equations:

$$[\dot{Ca^{2+}}]_i(t) = -\frac{[Ca^{2+}]_i}{\tau_{Ca^{2+}}} + [Ca^{2+}]_{spike}\sum_j \delta(t - t_{spike,i,j}) \tag{8}$$

$$[\dot{nNOS}]_i(t) = \frac{1}{\tau_{nNOS}}\left(\frac{[Ca^{2+}]_i^3}{[Ca^{2+}]_i^3 + 1} - [nNOS]_i\right) \tag{9}$$

$$[\dot{NO}](\mathbf{x},t) = -\lambda[NO] + D\nabla^2[NO] + \sum_i \delta^2(\mathbf{x} - \mathbf{x}_i)[nNOS]_i \tag{10}$$

$$\dot{V}_{t,i}(t) = \frac{[NO](\mathbf{r}_i,t) - [NO]_0}{[NO]_0 \tau_{V_t}} . \tag{11}$$

A depolarization within a nerve cell upon a spike-event t_{spike} causes a fixed inflow of ionic current $[Ca^{2+}]_{spike}$, which is modeled as an instantaneous increase of $[Ca^{2+}]$. The concentration decays exponentially by a time constant $\tau_{Ca^{2+}}$. Though Ca^{2+} currents can be described in a much more detailed fashion, it can be considered as a reasonable approximation [20, p. 198-203]. The influence of $[Ca^{2+}]$ onto $[nNOS]$ was modeled by Sweeney et al. through (9) using the Hill equation [21] to model a cooperative binding mechanism. The rate of $[nNOS]$ is then fed into the "pool" of nitric oxide via point sources located at the neurons' positions. Diffusion of nitric oxide is modeled by a diffusive term with diffusion constant D. An additional decay with λ being the decay constant was added apart from the inflow and the diffusive term to provide a stable finite $[NO]$ concentration under constant neuronal activity.

Finally, the dynamics of firing thresholds $V_{t,i}$ were modeled such that the rate of change is proportional to the relative deviation of NO concentration at the neurons' locations from a global target concentration $[NO]_0$.

To acquire a target concentration $[NO]_0$ corresponding to the desired mean firing rate, we let the system run with the previous homeostatic mechanism, still solving (8)–(10) until a steady mean over the concentrations at the neurons' positions was reached. This mean was then set to be the target concentration and we switched to diffusive homeostasis. Table 3 summarizes the choice of parameters that were introduced in this section. Diffusion parameters roughly match those measured in experiments [22].

Simulation of diffusion

We solved (10) with the finite difference method on a grid $\mathbf{x}_{i,j}$ with a resolution of 100×100 points. Integration over time was carried out by a 4th-order Runge-Kutta

method with a time step of $1\,\text{ms}$. $\nabla^2 NO(\mathbf{x}_{i,j}) = \nabla^2 NO_{i,j}$ was approximated by

$$\nabla^2 NO_{i,j} \approx \frac{NO_{i+1,j} + NO_{i-1,j} + NO_{i,j+1} + NO_{i,j-1} - 4NO_{i,j}}{h^2} \tag{12}$$

on each time step, where $h = L/100$ is the distance between neighboring grid points, determined by the length L of the square sheet and the resolution of the numeric grid. We implemented three possible boundary conditions:

1.) Neumann boundary conditions with $\nabla NO = (0,0)$ at the boundaries:

$$NO_{i,N_{\text{grid}}} = NO_{i,N_{\text{grid}}-2} \tag{13}$$
$$NO_{N_{\text{grid}},i} = NO_{N_{\text{grid}}-2,i} \tag{14}$$
$$NO_{i,-1} = NO_{i,1} \tag{15}$$
$$NO_{-1,i} = NO_{1,i} \ . \tag{16}$$

2.) Periodic boundary conditions:

$$NO_{i,N_{\text{grid}}} = NO_{i,0} \tag{17}$$
$$NO_{N_{\text{grid}},i} = NO_{0,i} \tag{18}$$
$$NO_{i,-1} = NO_{i,N_{\text{grid}}} \tag{19}$$
$$NO_{-1,i} = NO_{N_{\text{grid}},i} \tag{20}$$

with N_{grid} being the grid resolution.

3.) Dirichlet boundary conditions with $NO = NO_{\text{bound.}}$ at the boundaries.

Neumann boundary conditions were used for most of the simulations if not explicitly stated otherwise. This decision relates to the previously described mechanism of synaptic growth: Neurons placed close to the edge of the sheet have a lower probability of growing new connections with other neurons due to the absence of neighboring neurons in the direction perpendicular to the close-by border. This lack of proximity to other neurons decreases the chance of being selected randomly by the distance-dependent synapse generation mechanism, which favors connections between neurons with short distances. It therefore models the synaptic growth within a square "cutout" of neural tissue.

(10) describes the influx of [NO] as a sum of scaled and spatially shifted Dirac functions. Apart from the question whether this source term results in a well defined, finite analytic solution at the neurons' positions (see Section *Spatial configuration of neurons allows for the precise prediction of firing rates*), it can only be modeled to a certain degree of accuracy depending on the resolution of the numeric grid. In practice, we approximated the point sources of NO as insertions at individual grid cells at a rate of $[\text{nNOS}]_i(t)/h^2$, where the normalizing divisor h^2 ensured the desired total influx per neuron. This numeric implementation required two additional constraints: First, all random neuron positions were confined to integer multiples of h in x- and y-direction. Second, to avoid redundancy and for physiological reasons, each grid cell could only hold one neuron at maximum.

Software

The neural network was simulated in python using the BRIAN spiking neural network simulator package [23]. Plots were generated using the Matplotlib python package [24]. Fitting of the power-law exponent of synaptic lifetimes was done with the *powerlaw python package* [25], which uses a maximum-likelihood method to fit power-law exponents to the lifetime data.

Table 4. Diffusion constants and number of simulations used in Fig. 1E and F.

D [$\mu m^2 ms^{-1}$]	Number of Sim.
0.0	1
$0.1, 0.2, ..., 0.8, 0.9$	2
$1.0, 2.0, ..., 5.0, 8.0, 10.0, 15.0, 20.0$	4

Results

Diffusive homeostasis produces a broad distribution of firing rates

In a first set of analyses, we reproduced the finding from Sweeney et al. [10] that the diffusive homeostasis mechanism can produce a broad distribution of firing rates among the excitatory neurons. Fig. 1A–D compares the distribution of firing rates, comparing both homeostatic mechanisms. As expected, non-diffusive homeostasis led to a sharp distribution of firing rates at 3 Hz. Diffusive homeostasis indeed resulted in a much broader distribution of firing rates. In panel A, we found a skewness of $v_{diff.} = 0.765$ for diffusive homeostasis. To assess whether the statistics resemble a log-normal distribution, we also plotted the distribution of decadic logarithms of firing rates in Fig. 1B and D. Panel B shows the distribution of the decadic logarithms of excitatory firing rates, being well fitted by a normal distribution. Inhibitory firing rates were relatively unaffected by changing the homeostatic mechanism, see panels C and D.

Sweeney et al. found that diffusive homeostasis maintains the variance of the distribution of firing rates across a wide range of diffusion constants but rapidly approaching zero for small values (cf. [10], Fig. 3C). We were able to reproduce this result, see Fig. 1E. Homeostasis reaches a point of saturation, where faster diffusion has no effect on the heterogeneity of firing rates. Each of the data points in Fig. 1E and F corresponds to a single full simulation, though the same simulation data was used in A and B. 55 simulations were run in total. We picked the D-values by hand to achieve a good representation of the overall trend while limiting the number of simulations. The set of diffusion constants used is given in Table 4. We also investigated the influence of the diffusion constant on the distribution's skewness, shown in Fig. 1F, to further quantify this dependence. Compared to the standard deviation, we saw a similar but not as clear trend with a drop for very small diffusion constants, even occasionally resulting in a left-skewed distribution (negative D-values).

A naturally emerging question when altering the diffusion constant is how excitatory firing rates behave in the absolute limit of infinitely fast diffusion. In fact, this case is quite easy to implement in the simulation: One simply has to feed all NO sources into a single scalar variable of NO concentration. This then provided the same NO readout for all excitatory neurons, which means that all excitatory thresholds changed at the same rate all the time, only shifting their initial distribution. Therefore, the effect of this particalur distribution will remain present for the entire simulation, and a larger variance among excitatory thresholds will likely also broaden the distribution of firing rates. Even though the firing threshold is an abstract quantity and cannot be directly measured in biological neurons, analyses of neuronal voltage dynamics suggest that spike-initiation voltages in cortical neurons can vary on the order of tens of millivolts [26, 27]. For simplicity however, we chose to set all excitatory thresholds to the same initial value. Fig. 1A–D shows the distributions for this case. As one can see, this results in a similar but broader log-normal like distribution of excitatory firing rates, accompanied by a higher skewness of 1.51.
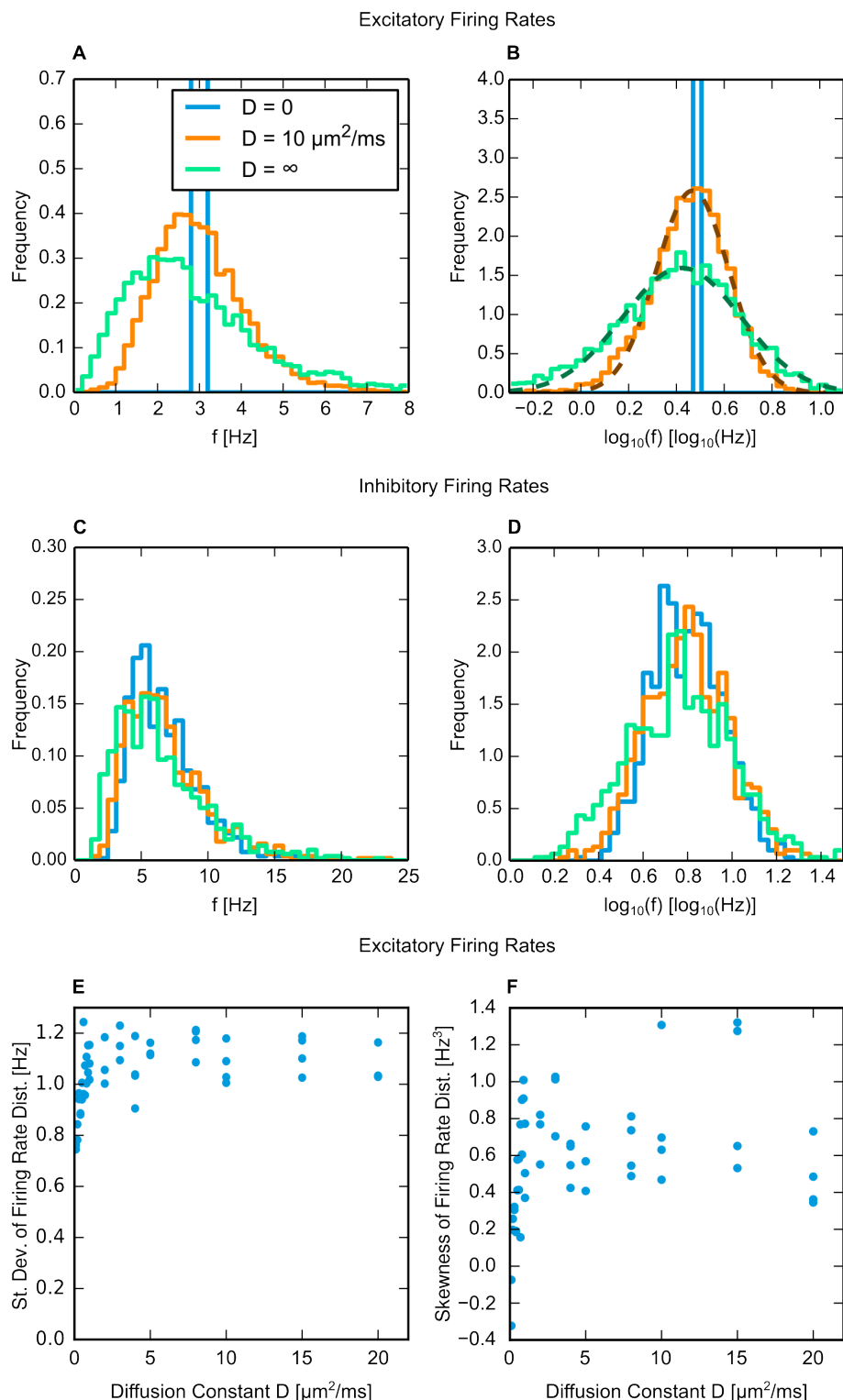
Fig 1. Distribution of firing rates. A,B,C,D: Empirical PDF of mean firing rates over the excitatory (A/B) and inhibitory (C/D) population in regular (A/C) and logarithmic space (B/D). Distributions were generated from 10 simulation runs, 1 simulation was used for non-diffusive homeostasis. Mean firing rates were calculated from spikes within $1000\,\mathrm{s} \leq t \leq 1500\,\mathrm{s}$. Dashed lines in B are Gaussian fits. **E,F**: Standard deviation (E) and skewness (F) of firing rate distribution of excitatory neurons. Each data point was generated from one full simulation.

Model produces non-random features of network topology and dynamics

While we explicitly intended altering the statistics of excitatory firing rates by implementing diffusive homeostasis, we wanted to preserve what has previously been reported by Miner and Triesch regarding the evolution and structure of recurrent excitatory weights [11]. More specifically, we were concerned with the following features of synaptic topology and dynamics: First, an overrepresentation of excitatory bidirectional connectivities, a feature found to be present in cortical networks [1]. Second, a power-law distribution of synaptic lifetimes. Loewenstein et al. reported on this feature in a study on the auditory cortex of mice [28]. Third, a heavy-tailed, log-normal like distribution of synaptic efficacies, which have been observed in a number of experimental studies [1, 2, 29, 30].

Fig. 2 summarizes the results regarding these properties. As shown in Fig. 2A and B, Diffusive homeostasis leads to the same stable level of recurrent excitatory connection fraction, as well as an over-representation of bidirectional connections. This over-representation is due to the distance-dependent probability of creating a new synapse between a pair of excitatory neurons [11, 31].

Fig. 2C shows that a log-normal like distribution of excitatory weights is preserved under diffusive homeostasis. Theoretical approaches to explaining this property are mainly based on a combination of multiplicative and additive weight dynamics [6, 28, 30, 32], which is in line with our implementation of multiplicative normalization and additive STDP. We did observe that the distribution is slightly left skewed. This is in line with results by Statman et al., namely that the distribution of synaptic spine sizes better fit the distribution of a simulated Kesten process than a log-normal distribution at the lower end of spine sizes, where the Kesten process also predicted higher probabilities [6].

Synaptic lifetimes have been shown to approximately follow a power law distribution in earlier versions of LIF-SORN and binary SORN [11, 32], where the synaptic lifetime is defined as the time between the generation and pruning of a synapse. Measuring the distribution of synaptic lifetimes is numerically challenging since a finite total simulation time leads to a falloff of probability for larger lifetimes. Furthermore, synapses whose lifetimes *could* have been potentially longer but were simply terminated by the end of the simulation will cause a bunching and over-representation of lifetimes within the time range given by the total simulation time. To our knowledge, there exists no general solution for the first problem other than running longer simulations. The second problem could be tackled by only including synapses into the statistics which terminated before the end of the simulation, though this reduces the size of the dataset. Practically, we accounted for this by only including lifetime periods into the statistics that explicitly contained an "on-off" transition in the end.

Another question we faced was which method of estimating the power-law exponent to use. It has been argued that a simple linear fit in log-log space can easily lead to wrong estimates due to large systematic errors, and common error estimates of the regression cannot be trivially interpreted [33, 34]. Clauset et al. have shown that the method of maximum likelihood estimation (MLE) provides a better framework for extracting power-law exponents [34]. We made use of the *powerlaw python package* [25, 35]. It provides a toolset for the analysis of potentially power-law distributed data, applying the maximum likelihood method as described by Clauset et al. [34]. An additional feature of this package—also originally proposed by Clauset et al.—is the possibility to automatically find a lower bound $x_{\min.}$ below which data points are discarded from the analysis, based on the goodness of the estimated power law to the actual data. The authors argue that this feature accounts for the possibility that smaller values of a dataset might not follow a power law as strictly as found in the tail

of the distribution. This optimization is based on the Kolmogorov-Smirnov statistic, which is the maximum absolute distance $d_{\max.}$ between the empirical cumulative distribution function of the data and the cumulative distribution function of the analytic prediction. It can be further used to perform a statistical test, allowing a judgment whether a given dataset of random variables was generated from the given PDF. To find the optimal value of $x_{\min.}$ however, the authors simply minimize $d_{\max.}$.

Observing the distribution of synaptic lifetimes, we found that fitting a power law to the simulation data would rather require to define an *upper* bound $x_{\max.}$ than a lower one, since we observed a negative deviation from the linear behavior in a log-log plot for large synaptic lifetimes, see Fig. 2D. The *powerlaw package* allows for manually setting an upper bound, but the optimization described before is only available for $x_{\min.}$. We therefore decided to manually implement the same approach for $x_{\max.}$, while keeping the lower bound fixed at $x_{\min.} = 1\,s$. We swept through values for $x_{\max.}$ within $2\,\mathrm{s} \leq x_{\max.} \leq 750\,\mathrm{s}$, with $750\,\mathrm{s}$ being the maximal possible synaptic lifetime to be recorded. We estimated the power-law exponent with the aforementioned package for each value of $x_{\max.}$ and calculated $d_{\max.}$. The value of $x_{\max.}$ resulting in the smallest $d_{\max.}^{min.}$ was then picked for the final estimation of the exponent. We did expect $d_{\max.}$ to go through a minimum for a certain value of $x_{\max.}$ and to increase again due to the statistical deviations for long lifetimes. We did not observe this behavior, however. Instead, $d_{\max.}$ was monotonically decreasing but converging. Therefore, we actually found its minimal value for $x_{\max.} = 750\,\mathrm{s}$ for both diffusive homeostasis and non-diffusive homeostasis ($d_{\max.,\mathrm{diff.}}^{min.} = 0.30$, $d_{\max.,\mathrm{non-diff.}}^{min.} = 0.34$). We thus accepted the values for α acquired by MLE for both entire datasets as valid, yielding slopes of -1.455 (standard error $5.52 \cdot 10^{-4}$) for diffusive homeostasis and -1.468 (standard error $5.70 \cdot 10^{-4}$) for non-diffusive homeostasis. The resulting exponents are slightly smaller than previously reported values of $\approx -5/3$ [11]. The precise slope of the power law has previously been related to the balance of potentiation and depression [11].

Heterogeneity of firing rate leads to the emergence of strongly influential excitatory neurons

Having established that the model accounts for above-chance bidirectional connectivities, a log-normal like distribution of recurrent excitatory weights and a power-law distribution of synaptic lifetimes in the same way as its predecessor, we sought for possible differences within our network topology as a result of diffusive homeostasis. Since we only implemented synaptic normalization for the sum of incoming weights, the total or average strength of *outgoing* connections may vary from cell to cell. In a sense, the strength of outgoing connections per neuron can be regarded as a measure of how influential a neuron's activity is with respect to other neurons in the network. Effenberger et al. have proposed a model where such "driver neurons" form highly active and interconnected subnetworks [36], an observation that is backed up by experimental studies [37, 38]. Fig. 3A shows that diffusive homeostasis allows for the emergence of a small group of highly influential neurons, which resembles the findings in [36]. A comparison of statistics generated with shuffled versions of the weight matrices shows that above-chance exceptionally strong mean outgoing weights were indeed present (two-sample Kolmogorov-Smirnov test, $p < 10^{-30}$). The fact that this effect is very pronounced in the case where D is neither zero nor infinite can be explained by considering that a non-zero but finite diffusion rate leads to a quenched disorder in firing rates: The random but fixed geometric configuration of neurons determines the firing rates of individual neurons via the homeostatic mechanism and this activity configuration is kept persistent throughout the simulation (see Section *Spatial configuration of neurons allows for the precise prediction of firing rates*). As we shall
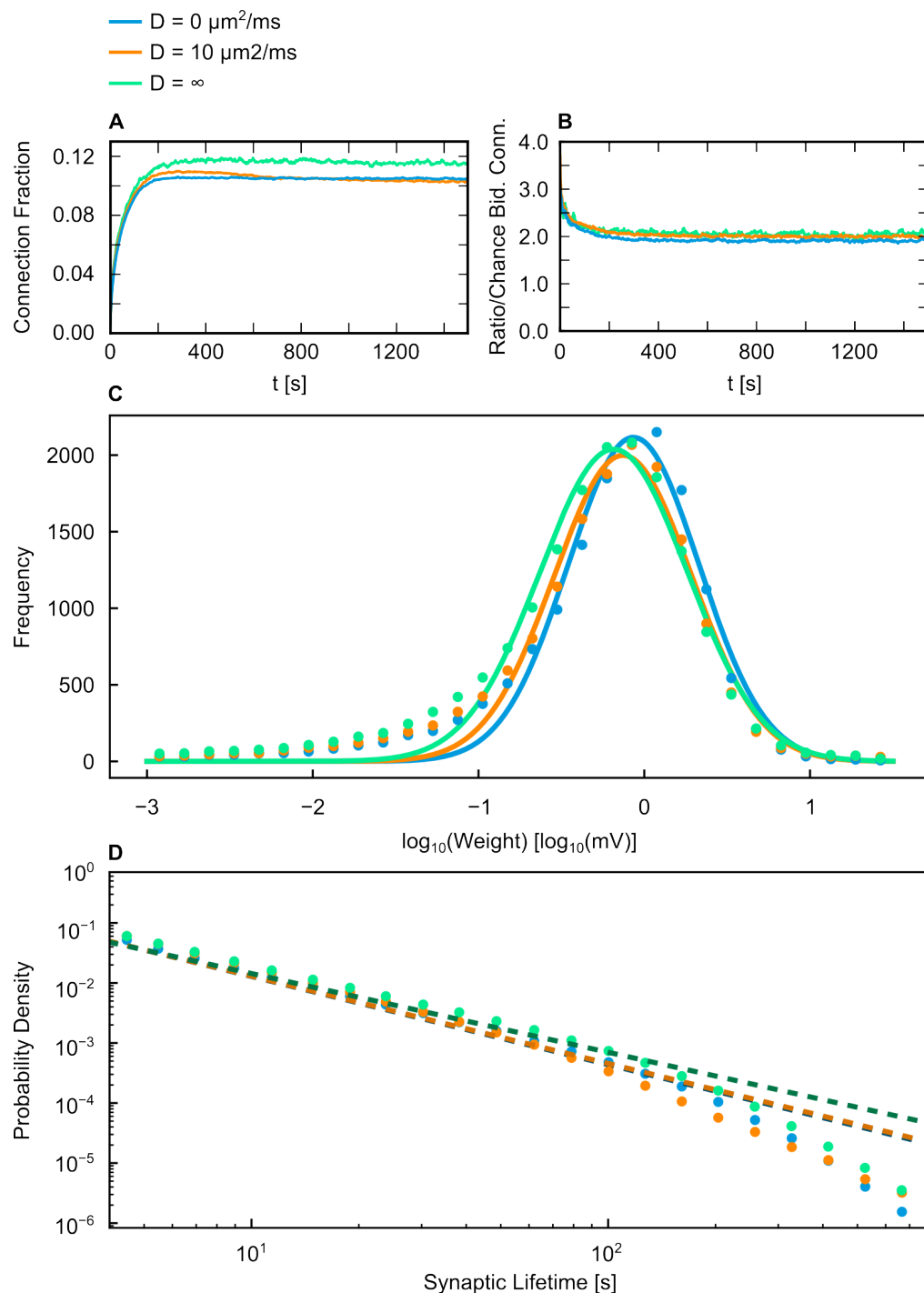
Fig 2. Structural and dynamic features of excitatory synaptic connectivity.
A: Evolution of recurrent excitatory connection fraction. **B**: Ratio of bidirectional connections relative to a random Erdős-Renyi graph. **C**: Distribution of excitatory recurrent weights after 1500 s. Solid curves are Gaussian fits. Data for each diffusion constant was taken from 5 simulations. **D**: Distribution of recurrent excitatory synaptic lifetimes (time between synapse generation and pruning). Single-trial data. Solid lines are estimates of a power-law exponent, giving a slope of approximately -1.9 for diffusive homeostasis and -1.7 for non-diffusive homeostasis. 5 simulation runs were used for each curve in panels A and B, panels C and D show representative single-trial data.
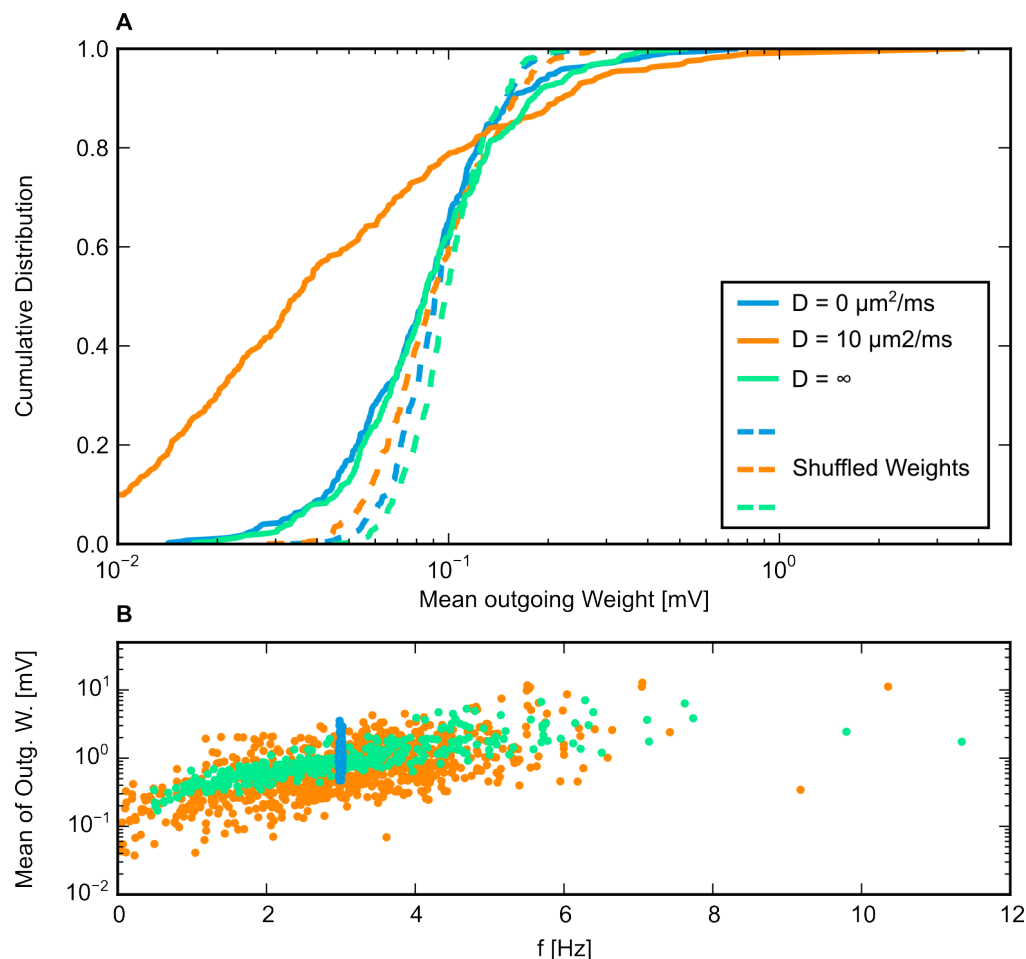
Fig 3. Presence of strongly influential neurons with high firing rates. A: Cumulative distribution of decadic logarithm of mean outgoing excitatory weights. Dashed lines are means obtained by randomly shuffling synaptic weights. Single trial data. **B**: Mean of outgoing excitatory weights at $t = 1500\,\mathrm{s}$ plotted against mean presynaptic firing rate (averaged over $700\,\mathrm{s} \leq t \leq 1000\,\mathrm{s}$) in logarithmic space. Each point corresponds to a presynaptic excitatory cell. Two simulation runs were used for diffusive homeostasis, all other are single-trial data.

discuss below, a persistent above-average firing activity leads to long-term potentiation. In contrast, instantaneous diffusion also allows for heterogeneous firing rates, but the correlation with the quenched disorder of the neurons' positions is lost and therefore the effect seen in Fig. 3A in the case of $D = 10\,\mu\mathrm{m}^2\mathrm{ms}^{-1}$ is attenuated for $D = \infty$.

Synapses between highly active presynaptic cells and postsynaptic neurons with lower activity are known to be subject to long-term potentiation [39, 40]. With this causal relation in mind, we argue that diffusive homeostasis effectively embodies a similar functional role as inhibitory STDP in [36] by allowing for the presence of excitatory cells with strongly above-average activity. We tested this relationship by plotting the mean outgoing weights against the average firing rate, see Fig. 3B. A strong heterogeneity of firing rates allowed for the development of few neurons with comparably strong mean outgoing weights, while the distribution of mean weights resulting from a narrow distribution is limited to a smaller range. We also tested the case of instantaneous diffusion. Mean weights did not reach as high values as in the case

of diffusion at a finite rate. This is in line with our previous remark that, though instantaneous diffusion also exhibits heterogeneous firing rates, this heterogeneity is not linked to the spatial disorder of the neurons' positions which are fixed over time.

Experimental studies have not only considered the presence of neurons with strong influence onto other neurons [38], but also found evidence that highly active neurons form subnetworks with an increased connectivity, in the sense that these cells are more likely than average to connect to each other, see [37]. We tested this in our network by evaluating the connection fraction among the top 10% of excitatory neurons with respect to their average firing rate within $1000\,\mathrm{s} \leq t \leq 1500\,\mathrm{s}$ and comparing it to the rest of the excitatory population and the same calculation for the non-diffusive case. This returned CF $= 0.1371 \pm 0.0061$ for the top 10% and CF $= 0.0982 \pm 0.0013$ for the lower 90% in the case of diffusive homeostasis, and CF $= 0.0954 \pm 0.0044$ for the top 10% and CF $= 0.0992 \pm 0.0002$ for the lower 90% in the case of non-diffusive homeostasis. Standard errors were calculated from 5 simulation runs for each homeostatic mechanism, and connectivity matrices were taken from $t = 1500\,\mathrm{s}$. We concluded that a significantly higher connection fraction could be observed among neurons with above-average firing rates, and this difference was significant only in the case of diffusive homeostasis (Welch's t-test, p $= 3.87 \times 10^{-3}$ for diffusive homeostasis, p $= 0.48$ for non-diffusive homeostasis). Effenberger et al. reported a similar effect, in fact with even more pronounced differences of connectivity [36].

Spatial configuration of neurons allows for the precise prediction of firing rates

Having analyzed the distribution of firing rates resulting from the implementation of diffusive homeostasis, we were interested in how strongly the actual positioning of excitatory neurons influences the resulting statistics of firing activity. To do so, we assumed that the spontaneous firing measured during the stable phase of the network, characterized by a constant excitatory connection fraction, can be regarded as a homeostatic steady state. Given no sudden strong changes of neural input, the homeostatic feedback levels out the error signal, given by $[\mathrm{NO}] - [\mathrm{NO}]_0$ to approximately zero. Our search for the steady-state configuration of firing rates thus reduced to finding a set of firing rates that led to a concentration level of $[\mathrm{NO}]_0$ at every excitatory neuron's position:

$$[\mathrm{NO}](\mathbf{x}_i) = [\mathrm{NO}]_0 \, , \, \forall i \, . \tag{21}$$

Furthermore, we found that the nonlinearity between spiking activity and NO synthesis could be well approximated by a linear relation between average firing rate r_i and rate of NO synthesis $nNOS_i$ by

$$[\mathrm{nNOS}]_i = \frac{[\mathrm{Ca}^{2+}]_{\mathrm{spike}}^3 \tau_{\mathrm{Ca}^{2+}} \ln(2)}{3} r_i \equiv \gamma r_i \, . \tag{22}$$

See Appendix S1 for a derivation of the proportionality factor. Given this simplification, the steady state of NO concentration is thus defined by the solution of

$$0 = -\lambda[\mathrm{NO}] + D\nabla^2[\mathrm{NO}] + \sum_i \delta^2(\mathbf{x} - \mathbf{x}_i)\gamma r_i \tag{23}$$

which can be reformulated to

$$\left(\nabla^2 + \left(i\sqrt{\frac{\lambda}{D}}\right)^2\right)[\mathrm{NO}] = \sum_i \delta^2(\mathbf{x} - \mathbf{x}_i)\frac{-\gamma r_i}{D} \tag{24}$$

which is a two-dimensional Helmholtz equation. Its Green's function is

$$[\text{NO}](\mathbf{x}) = \frac{r_i \gamma}{2\pi D} K_0 \left(|\mathbf{x}| \sqrt{\frac{\lambda}{D}} \right) \equiv r_i \psi_{\text{point}}(|\mathbf{x}|) \tag{25}$$

where K_0 is the zeroth modified Bessel function of the second kind [41]. This solution reveals a fundamental problem of modeling the sources of NO production as point sources: the fact that $K_0(x)$ diverges to infinity for $x \to 0$. It is merely due to the finite density of the numeric grid used for the simulation of diffusion that allows for a finite target value of concentration.

Generally speaking, no matter how the actual shape of the numeric solution in the equilibrium at a constant production rate looks like, it must be of the form

$$[\text{NO}]_i(\mathbf{x}) = r_i \psi(|\mathbf{x}_i - \mathbf{x}|) . \tag{26}$$

The full solution is then

$$[\text{NO}](\mathbf{x}) = \sum_i [\text{NO}]_i(\mathbf{x}) . \tag{27}$$

By defining

$$\psi_{ij} \equiv \psi_{ji} \equiv \psi(|\mathbf{x}_i - \mathbf{x}_j|) \tag{28}$$

we could express condition (21) as

$$\sum_j \psi_{ij} r_j = [\text{NO}]_0 \tag{29}$$

or, as an operator

$$\hat{\psi}\mathbf{r} = [\text{NO}]_0 \mathbf{n} \tag{30}$$

$$\mathbf{n} \equiv (1, 1, ..., 1) . \tag{31}$$

The problem of finding the steady-state solution of the homeostatic constraint thus reduced to inverting $\hat{\psi}$:

$$\mathbf{r} = [\text{NO}]_0 \hat{\psi}^{-1} \mathbf{n} . \tag{32}$$

Still, we had to find a modified, non-diverging version of $\psi(\text{d}(\mathbf{x}_{\text{neur.},i}, \mathbf{x}))$ to acquire any prediction from this model. It had to retain the shape given by (25) for larger distances but approach the correct numeric error value at the origin, determined by the spacing of the numeric grid. We solved this problem by the following expression:

$$\psi_{\text{approx.}} \equiv \frac{1}{\left(\frac{1}{\psi_0^\varepsilon} + \frac{1}{\psi_{\text{point}}^\varepsilon} \right)^{\frac{1}{\varepsilon}}} \tag{33}$$

where ψ_{point} is the analytic solution for a point source, ψ_0 is the maximum value appearing in the numeric simulation and ε determines the "smoothness" of transition between ψ_{point} and ψ_0. We chose $\varepsilon = 10$ for all further calculations. We took the simple approach of interpreting this value as a mean of the analytic solution across the area covered by the corresponding grid cell to find an expression for ψ_0. As an additional simplification, we substituted the necessary integration over the square grid cell by a circular area of equal size around the source. This calculation yielded

$$\psi_0 = \gamma \frac{1 - h\sqrt{\frac{\lambda}{\pi D}} K_1 \left(h\sqrt{\frac{\lambda}{\pi D}} \right)}{h^2 \lambda} \tag{34}$$

where h is the spatial resolution of the grid cells and K_1 the first modified Bessel function.

By simply calculating all matrix elements of $\hat{\psi}$ by means of (28), one would neglect the finite boundaries of the system, which would cause neurons close to the edge to "bleed" into empty space. We accommodated for zero-flux Neumann boundary conditions by adding appropriately mirrored copies of the neurons' positions, canceling the orthogonal component of the gradient at the boundaries.

After having worked out the analytical basis, we compared the prediction obtained from numerically solving (30) for certain spatial configurations of neurons to the steady-state firing rates of the full spiking network with the same spatial structure. As Fig. 4A shows, the actual shape of the distribution was well predicted by the solution of the linear system. Furthermore, we were particularly interested in the quality of the predictions with respect to the choice of diffusion constant. Fig. 4B shows three examples: For $D = 10\,\mu m^2 ms^{-1}$, the correlation between measured and predicted firing rates is very good. In contrast, we included the — obviously unsuccessful — attempt to predict firing rates for a simulation with instantaneous diffusion based on the spatial structure by setting D to a relatively high value of $D = 100\,\mu m^2 ms^{-1}$. This represented a limiting case where our analytic model could not make any meaningful predictions, since instantaneous diffusion overrides any spatial inhomogeneities. The outcome of the third case shown in the plot, $D = 0$, is correctly predicted by the analytic model. In general, instantaneous diffusion as well as $D = 0$ overrode the effects of spatial heterogeneity onto firing rates.

These observations naturally led us to the question of how the correlation between predicted and measured firing rates behaves in between the aforementioned limits. Especially, we were interested in the range of the diffusion constant for which our model provides a good description of the full spiking network's activity. Fig. 4C depicts the Pearson correlation coefficient of $f_{matrix,predict.}$ and $f_{sim.}$ against the diffusion constant used in the simulation. A relatively high correlation was obtained for a wide range of diffusion constants. However, we could see a general decline of correlation for larger diffusion constants. This trend was in line with the aforementioned limit of instantaneous diffusion, namely a complete decorrelation between prediction and measurement, as well as the good agreement for $D = 10\,\mu m^2 ms^{-1}$ shown in Fig. 4A.

Having acknowledged the good agreement between the full network simulation and the predictions of our simplified model, we also made predictions for more realistic settings of spatial densities. Although neuronal densities can vary considerably across different cortical areas and species [42], we considered a density of $9 \times 10^4\,mm^{-3}$ as a realistic value [43]. This corresponds to a mean free path of 22.31μm. On a single two-dimensional slice of $1000\,\mu m \times 1000\,\mu m$, one should therefore populate approximately 2000 neurons to achieve the same mean free path. For the sake of a larger sample set, we calculated the homeostatic equilibrium for 8000 randomly placed cells on a $2000\,\mu m \times 2000\,\mu m$ sheet. As shown in Fig. 5 (blue histogram), this resulted in an equally shaped, skewed distribution of firing rates.

Two other variants of diffusion and cell placement are also shown in Fig. 5: 9×10^4 randomly placed cells in a cube of $1\,mm^3$, and a single, flat layer of 8000 cells (random x- and y-position, fixed z-coordinate) in a $2000\,\mu m \times 2000\,\mu m \times 1000\,\mu m$ cuboid. While the former case mimics a uniform neuronal structure, the latter was meant to mimic interaction solely across a single cortical layer. All other diffusion parameters (λ and D) were kept at their standard values. The resulting firing rate distributions are depicted in Fig. 5. Both variants in 3D space yielded similar distributions, which, however, differed from the original setup with respect to variance and skewness, both being reduced.

Given the good predictions of firing rates of our simplified mathematical model under the standard configuration, these additional predictions suggest the
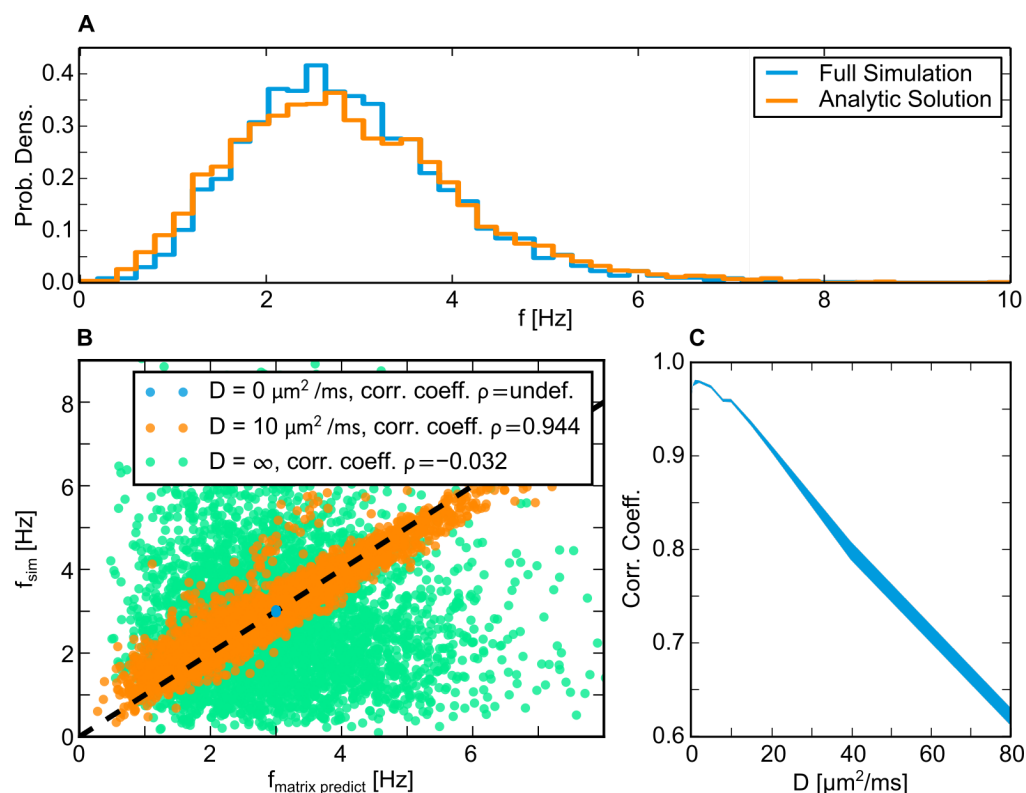
Fig 4. Empirical distribution of excitatory firing rates and theoretical prediction. A: Distribution of firing rates for $D = 10\,\mu m^2 ms^{-1}$, full simulation and analytic prediction. Data was taken from 10 simulation runs. **B**: Measured firing rates ($1000\,s \leq t \leq 1500\,s$) versus predicted firing rates based on the solution of (30). For $D = \infty$ (instantaneous diffusion in the full simulation), the analytic prediction was calculated with a comparably large diffusion constant of $D = 100\,\mu m^2 ms^{-1}$. Plot shows representative single-trial data. **C**: Pearson correlation coefficient of predicted and measured firing rates versus diffusion constant. Line width depicts standard error, 5 simulations were used for each D-value.
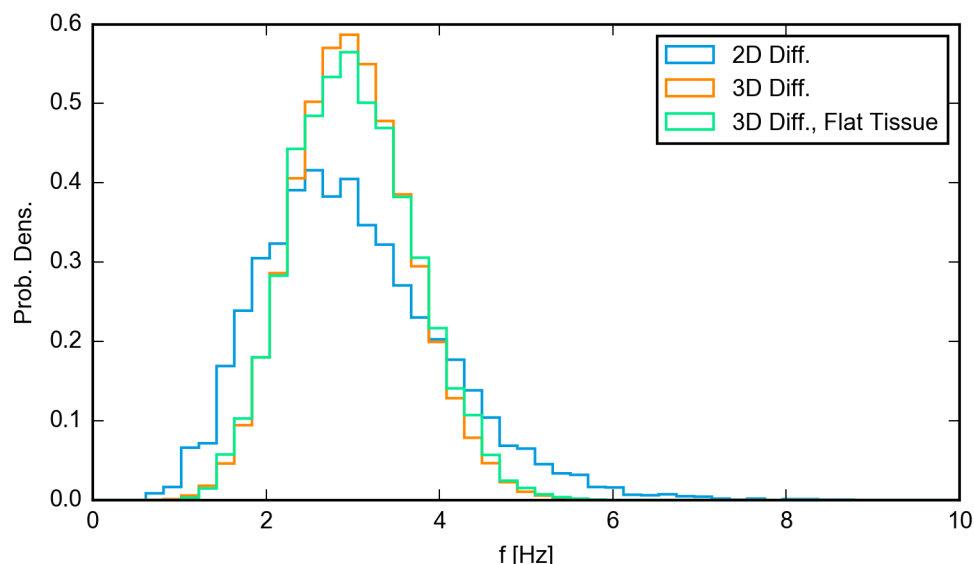
Fig 5. Distribution of firing rates acquired by solving the diffusive homeostatic fixed point. 2D variant was carried out on a $2000\,\mu\text{m} \times 2000\,\mu\text{m}$ sheet (grid resolution 200×200) and 8000 randomly picked cell positions. 3D variant used a $1000\,\mu\text{m} \times 1000\,\mu\text{m} \times 1000\,\mu\text{m}$ cube (grid resolution $100 \times 100 \times 100$) and 9×10^4 random cell positions. The 3D variant with a flat neural tissue used a $2000\,\mu\text{m} \times 2000\,\mu\text{m} \times 1000\,\mu\text{m}$ cube (grid resolution $200 \times 200 \times 100$) and 8000 cell positions with random x- and y-coordinates and a z-coordinate fixed at $500\,\mu\text{m}$. All graphs depict single-trial data.

implementation of a full network simulation combined with 3D diffusion for further testing of the homeostatic model. Apparently, the fact that diffusion in three dimensions results in a more localized fundamental solution of a single point source compared to two dimensions leads to a reduced intercellular overlay of homeostatic signals. We also noticed that the width of the distributions could not be further broadened artificially by increasing the the diffusion constant to very high values.

We also performed systematic tests to see how increasing the diffusion constant (which is equivalent to increasing neural densities) affects the second and third moments of the firing rate distribution. Fig. 6 shows that indeed neither variance nor skewness can be increased further than a certain saturation value.

Low-density neighborhoods correlate with strong outgoing connections

We previously stated that diffusive homeostasis allowed the network to develop few neurons with exceptionally strong outgoing weights. We found this effect to be present in neurons with a highly above-average firing rate. Moreover, our analytical predictions of individual neuronal activity suggest that the steady state of firing rates is strongly influenced by the spatial structure of excitatory neurons. Combining these two qualities led us to the conclusion that one should be able to observe some relation between spatial structure and the emergence of "driver neurons". More specifically, regions of neurons with above average firing rates should develop stronger outgoing connections. We approximated the local neuron density by means of a Gaussian kernel with $\sigma = 50\,\mu\text{m}$ to test this hypothesis. Fig. 7 shows the results. Despite a certain amount of randomness,
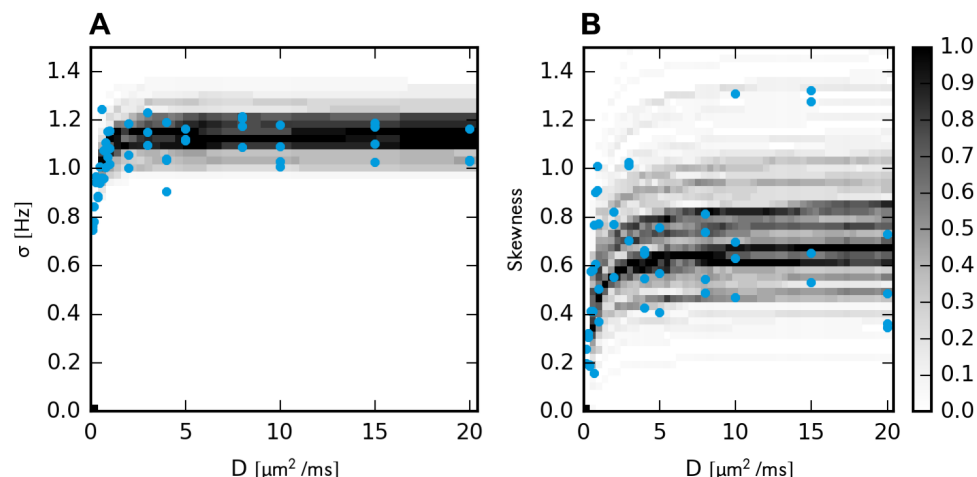
Fig 6. Standard deviation and skewness of firing rates saturate for fast diffusion. Comparison of distribution of standard deviation (**A**) and skewness (**B**) for random-matrix solutions (gray) and values acquired from simulation (blue), with Neumann boundary conditions. each blue dot represents a single simulation. The histograms for the analytic solutions were generated for 50 D values, spanning equally between $D = 0$ μm²/ms and $D = 20$ μm²/ms. Each column is a histogram of 200 firing-rate solutions for randomly generated positions, giving a total of 10000 matrix solutions.

our prediction was indeed verified. In particular, it is interesting to see that spatially separated neurons are able to acquire strong outgoing weights despite the fact that the distance-dependent connection probability in our model does not favor connections coming from neurons with larger distances to neighboring cells. Also, one should bear in mind that we can not expect the correlation observed in Fig. 7B to be larger than in the relation shown in Fig. 3D, since the former depends implicitly on the latter.

Experimental Evidence For Correlation Between Neural Density and Neural Activity

Considering the prediction that the local inverse neural density should correlate with firing rates of individual neurons, see Fig. 7C, we searched for available experimental data that would be suitable to test this prediction. A dataset by Gonçalves et al. provides calcium imaging recordings from spontaneous activity in Layer 2/3 mouse somatosensory cortex during different developmental stages, including spatial distance matrices and estimated firing rates [44, 45]. Using a Gaussian kernel density estimation on data from postnatal days 30–40, we found a significant correlation between inverse neural density and firing rates, see Fig 8. We chose the width of the Gaussian kernel to be the average distance to the nearest neighboring cell in the dataset, which was approximately 10μm. Slight variations of the kernel width did not affect the significance of the correlation.

The Allen Brain Institute also provides a large number of datasets of mouse brain recordings, including calcium imaging data that allows to extract neurons' positions as well as their activity [46]. Analyzing multiple datasets from this database, we could not find significant evidence for a correlation between neural density and firing rates. We hypothesize that this lack of correlation is due to the fact that recordings were taken
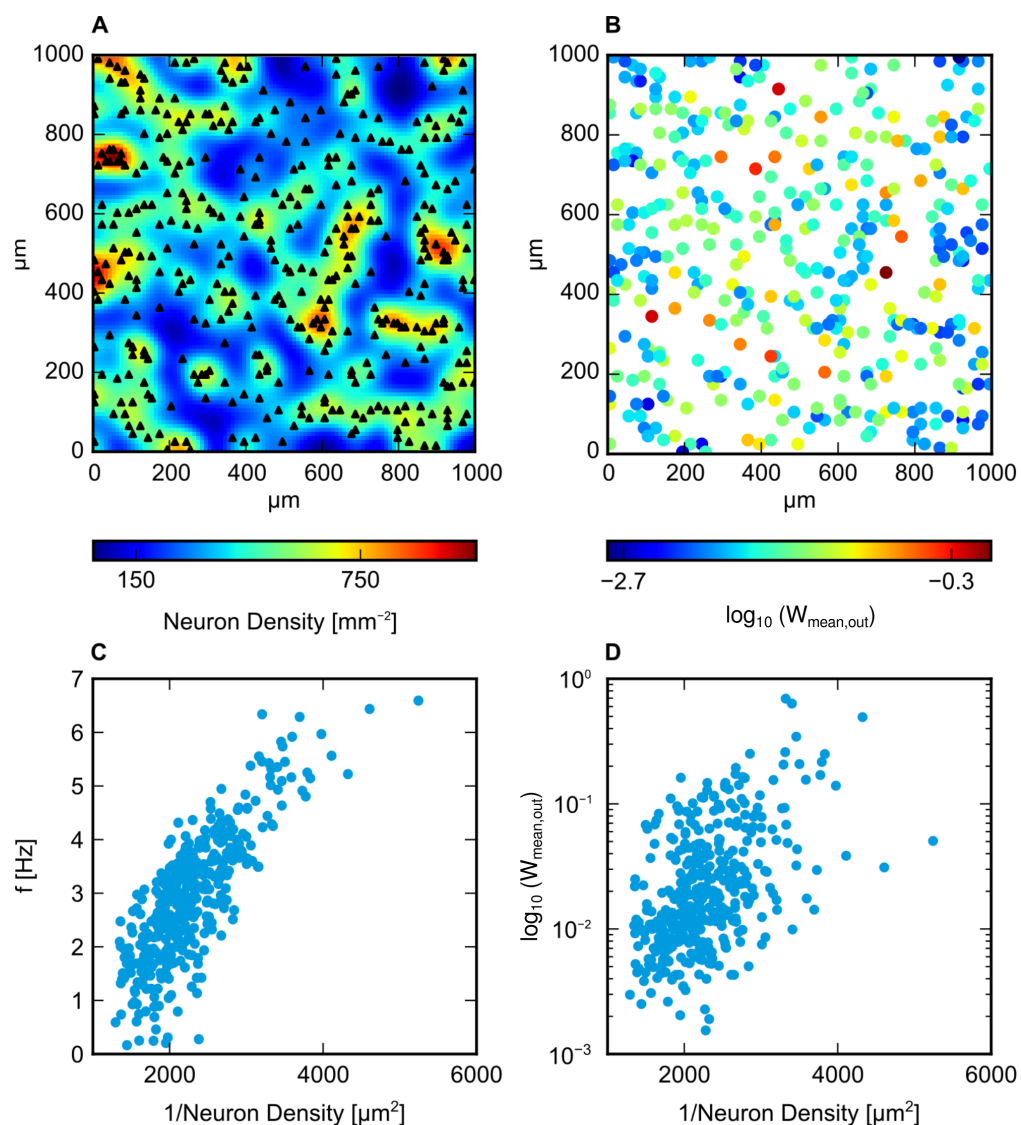
Fig 7. Mean outgoing excitatory weights vs. reciprocal neuron density. A: Illustration of excitatory neurons' positions and local neuron density (calculated by convolution with a Gaussian kernel with $\sigma = 50\,\mu\mathrm{m}$). **B**: Decadic logarithm of mean outgoing excitatory weights (mean over nonzero outgoing excitatory connections). Note the spatial correlation between **A** and **B** in high/low-density regions. **C**: Firing rate of excitatory neurons (averaged over $1000\,\mathrm{s} \leq t \leq 1500\,\mathrm{s}$) versus reciprocal neuronal density (same estimation method as in **A**). Coefficient of correlation $\rho = 0.798$. **D**: Decadic logarithm of mean outgoing excitatory weights (mean over nonzero outgoing excitatory connections) versus reciprocal neuronal density. Coefficient of correlation $\rho = 0.513$.
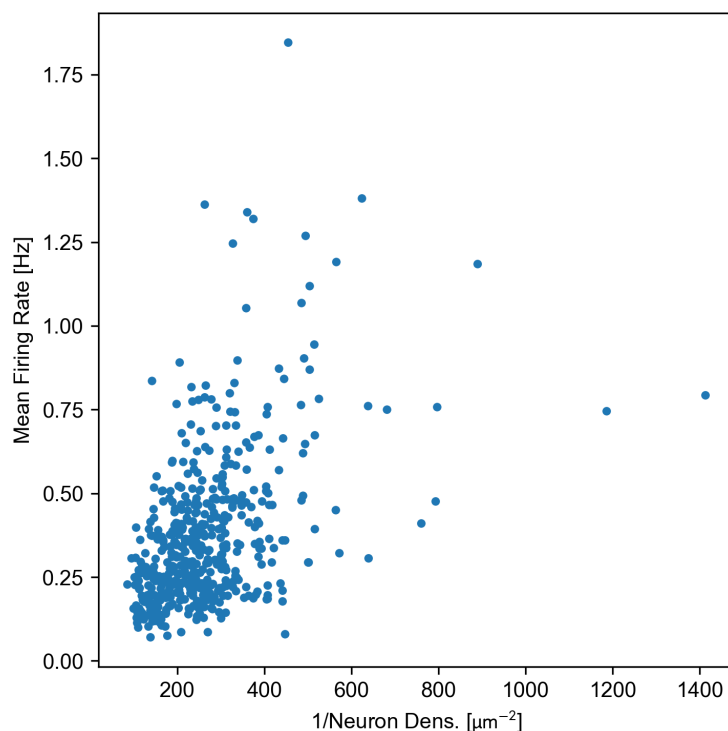
Fig 8. Inverse neural density vs. firing rates in mouse somatosensory cortex. Data was taken from [44, 45], using preprocessed data from calcium imaging recordings in Layer 2/3 mouse somatosensory cortex, postnatal days 30–40. Pearson correlation $\rho_{\mathrm{pears}} = 0.47$, p-value testing for non-correlation $p_{\mathrm{pears}} = 0.82 \cdot 10^{-28}$. Spearman correlation $\rho_{\mathrm{spear}} = 0.44$, p-value testing for non-correlation $p_{\mathrm{spear}} = 0.37 \cdot 10^{-24}$.

from visual cortex while the mice were presented with visual stimuli, which are likely to transiently change the activity patterns of the recorded neurons.

Discussion

The LIF-SORN in combination with diffusive homeostasis presents itself as a *self-organizing* model of cortical activity and plasticity to exhibit core features of neuronal firing statistics as well as synaptic connectivity and dynamics. In order to acquire a deeper understanding of the mechanisms that determine neuronal activity we developed a theory that allowed us to reliably predict the steady-state of firing rates based on the spatial configuration of excitatory neurons. We would like to emphasize that this explanation differs from common approaches of understanding the emergence of heavy-tailed statistics of firing rates in recurrent networks. Theoretical studies on the behavior of recurrent networks are largely based on the assumption that the excitability of neurons is not individually fine-tuned but rather randomly distributed and adjusted globally to achieve a desired mean firing rate. Predictions about the resulting activity are then made based on (potentially simplified) statistical features of recurrent connectivity and/or the specific form of the neuronal transfer function used in the model, see e.g. [47–49]. Our interpretation of our results led us to the conclusion that this approach matches the limiting case of instantaneous diffusion: While Fig. 1A–D did

not reveal many differences between finite-velocity and instantaneous diffusion in terms of overall statistics, the decorrelation shown in Fig. 4C suggests that increasing the diffusion constant goes along with a transition between a spatially determined configuration of excitatory firing rates and a network topology-determined behavior.

Naturally, this raises the question of biological plausibility. To our knowledge, no experimental study exists that relates measurements of spontaneous activity to local fluctuations of neuronal densities. However, our own analysis of available data revealed at least one experimental dataset that showed a significant relation between density and firing rates. We believe that this effect could not be observed robustly in a multitude of datasets due to a number of reasons which we shall discuss briefly.

First, we should consider the fact that calcium imaging of neurons is only capable of showing a planar section within the tissue. However, relating this to our hypothesis, it is important that neurons above or below the focal plane also affect those neurons being recorded via diffusive homeostasis. Therefore, a planar recording cannot provide the full spatial geometry that would be necessary for making an optimal prediction of neural activity. Moreover, neurons at the border of the recorded image region are most likely affected by neurons that are outside the recording frame. For a precise prediction of rates however, those ones should also be taken into account. A simple way to deal with this would be to exclude neurons in the outer region of the recording zone from the analysis. However, this could reduce statistical power.

A possible reason for the strong influence of spatial structure in the implemented model could be the fact that cells were modeled as approximate point sources of nitric oxide. This allowed for a clear distinction between individual cells, even in close vicinity. While Sweeney et al. argued that the size of the studied tissue is large compared to the size of individual somata (which, apparently, they claim to be the main source of nitric oxide), Philippides et al. reported that NO is often synthesized in a more delocalized way by means of fine fibers originating from the soma [50]. The diameter of these "production areas" is on the order of $10 - 100\,\mu$m. This suggests that diffusive homeostasis may not act as much as a precise tuner of single neuron activities as found in the computational model. Another possible flaw of the homeostatic model is the linear dynamics of thresholds with respect to the nitric oxide concentration, which is an ad-hoc assumption taken from the Sweeney et al. paper. Maybe nitric oxide affects excitability in a nonlinear way, preventing extreme deviations from a desired level of activity, but being much less sensitive to subtle changes of concentration.

Considering the possibility that diffusive homeostasis in the brain is not as exact in tuning neurons for a certain concentration, the actual network structure might also have an effect on activity that counters the effects of diffusive homeostasis, namely that spatial proximity between neurons also increases the chance of those neurons to be highly connected, which could lead to local clique excitation.

Interestingly, measurements in the barrel cortex and hippocampus have found that firing rates during exploration or task performance are significantly correlated with those found for spontaneous, baseline activity [8,51]. This suggests that the same set of neurons tend to be relatively active or inactive under different stimuli and changing environments. In the light of these observations, one might speculate whether random spatial positioning might at least partially act as a determinant of these individual working points of firing activity. We have shown that the predictions of our analytic approach to obtaining neuronal firing rates are consistent when using more realistic two-dimensional neuronal densities. Interestingly, the predictions for three-dimensional spatial interaction led to a smaller width and skewness of the resulting firing rate distribution. Still, since some amount of heterogeneity could still be observed, we consider it possible that local clustering or isolation of neurons can induce a disposition towards lower/higher long-term firing rates.

The basic assumption that has to be made for this prediction to hold is that NO concentrations are tuned towards a target concentration across neuronal cell bodies. In the theoretical model we used, this was achieved by tuning neuronal excitability by means of a perfect integral control. This might be considered an oversimplification, but does reflect the general idea that NO concentrations must be held within some regime associated with normal neuronal activity. In consequence, it is reasonable to assume that the aforementioned implications of varying neuronal densities still hold at least qualitatively, even if the tuning of NO concentration is not as strict and exact as seen in the theoretical model.

In a recent experimental study, Hengen et al. suggested the existence of "homeostatic mechanisms that regulate mean firing around cell-autonomous set points" [9]. By means of our analytic predictions regarding homeostatic set points, we have shown that diffusive homeostasis — in combination with random positioning of cell bodies — could provide an explanation for these heterogeneous and cell-specific set points of firing rates. However, the study also found that homeostatic regulation is suppressed during sleep. If and how this effect could possibly be incorporated into a model network subject to diffusive homeostasis remains to be clarified.

Despite these considerations regarding the effects of spatial structure onto individual firing rates, our modifications seem to be a plausible way of giving rise to many features of cortical structure and activity. Apart from the previously discussed properties of spiking activity, we have have shown that important features of synaptic topology and plasticity found in earlier research are compatible with diffusive homeostasis. We thereby created a model, which combines the here presented features of cortical structure with the desired statistics of neuronal activity. This was achieved without specific modifications of Hebbian plasticity rules, which have also been proposed as an explanation for log-normally distributed synaptic weights [7, 36, 49]. Sweeney et al. also included synaptic plasticity via STDP into their model, but did not include synaptic normalization, which led to a bimodal distribution of weights, instead of the log-normal like shape obsered in our model [10].

Recent studies have brought up inhibitory-to-excitatory STDP with respect to stabilizing network activity [52, 53]. Results similar to ours concerning network topology have also been achieved with inhibitory STDP [36]. In terms of their functional role of stabilizing network activity, it is reasonable to assume that both, diffusive homeostasis and inhibitory STDP, can simultaneously act in a biological system.

In addition, we found that heterogeneity of firing rates led to a much more pronounced separation of mean outgoing weights in our network, which were positively correlated to presynaptic firing rates. This is in line with other theoretical and experimental observations, arguing that a small subset of highly active neurons may serve to form relatively strongly connected and stable subnetworks that can quickly react to momentary changes in the environment, while fine tuned adaptation involves the slower firing majority of cells [4, 37, 54]. While our observations regarding the influence of diffusive homeostasis onto the network topology can be regarded as an indirect effect, Sweeney and Clopath also investigated the possibility that the diffusion of neurotransmitters could directly affect the dynamics of neural plasticity in a recent theoretical study [55], concluding that this promotes stronger synaptic weights between spatially close neurons. It is not clear whether this effect might interfere with our results in a model that combines the effects of diffusive neurotransmitters onto intrinsic, as well as synaptic plasticity: arguing within the scope of our model, two excitatory neurons close to each other will both approximately exhibit half of the firing rate that a single neuron at the same location would have. One could argue that this decrease in activity impedes their probability to form a strong synaptic connection. Future research might therefore involve the implementation of a combined diffusion model to check for

these possible interdependencies. [642]

As mentioned previously, models from the SORN family have also proven their [643] capabilities in associative learning and inference tasks [56]. A logical next step should [644] thus be to test whether the new features presented in this paper can enhance [645] performance in learning, in the sense that the computational and memory resources [646] given by the network size are used more efficiently. [647]

References

1. Song S, Sjöström PJ, Reigl M, Nelson S, Chklovskii DB. Highly Nonrandom Features of Synaptic Connectivity in Local Cortical Circuits. PLOS Biology. 2005;3(3). doi:10.1371/journal.pbio.0030068.

2. Lefort S, Tomm C, Floyd Sarria JC, Petersen CCH. The Excitatory Neuronal Network of the C2 Barrel Column in Mouse Primary Somatosensory Cortex. Neuron. 2009;61(2):301–316. doi:10.1016/j.neuron.2008.12.020.

3. Buzsáki G, Geisler C, Henze DA, Wang XJ. Interneuron Diversity series: Circuit complexity and axon wiring economy of cortical interneurons. Trends in Neurosciences. 2004;27.

4. Buzsáki G, Mizuseki K. The log-dynamic brain: how skewed distributions affect network operations. Nature Reviews Neuroscience. 2014;.

5. Marsat G, Maler L. Neural Heterogeneity and Efficient Population Codes for Communication Signals. Journal of Neurophysiology. 2010;104(5):2543–2555. doi:10.1152/jn.00256.2010.

6. Statman A, Kaufman M, Minerbi A, Ziv NE, Brenner N. Synaptic Size Dynamics as an Effectively Stochastic Process. PLOS Computational Biology. 2014;10(10):1–17. doi:10.1371/journal.pcbi.1003846.

7. Gilson M, Fukai T. Stability versus Neuronal Specialization for STDP: Long-Tail Weight Distributions Solve the Dilemma. PLOS ONE. 2011;6(10):1–18. doi:10.1371/journal.pone.0025339.

8. Mizuseki K, Buzsáki G. Preconfigured, skewed distribution of firing rates in the hippocampus and entorhinal cortex. Cell Reports. 2013;4.

9. Hengen KB, Torrado Pacheco A, McGregor JN, Van Hooser SD, Turrigiano GG. Neuronal Firing Rate Homeostasis Is Inhibited by Sleep and Promoted by Wake. Cell. 2016;165(1):180–191. doi:10.1016/j.cell.2016.01.046.

10. Sweeney Y, Kotaleski JH, Hennig MH. A Diffusive Homeostatic Signal Maintains Neural Heterogeneity and Responsiveness in Cortical Networks. PLoS Computational Biology. 2015;.

11. Miner D, Triesch J. Plasticity-Driven Self-Organization under Topological Constraints Accounts for Non-Random Features of Cortical Synaptic Wiring. PLoS Computational Biology. 2016;.

12. Zhang LI, Tao HW, Holt CE, Harris WA, Poo M. A critical window for cooperation and competition among developing retinotectal synapses. Nature. 1998;395:37–44.

13. Bi G, Poo M. Synaptic Modifications in Cultured Hippocampal Neurons: Dependence on Spike Timing, Synaptic Strength, and Postsynaptic Cell Type. The Journal of Neuroscience. 1998;18(24):10464–10472.

14. Froemke RC, Poo M, Dan Y. Spike-timing-dependent synaptic plasticity depends on dendritic location. Nature. 2005;434(7030):221–225.

15. van Rossum MCW, Bi GQ, Turrigiano GG. Stable Hebbian Learning from Spike Timing-Dependent Plasticity. Journal of Neuroscience. 2000;20(23):8812–8821.

16. Markram H, Wang Y, Tsodyks M. Differential signaling via the same axon of neocortical pyramidal neurons. Proceedings of the National Academy of Sciences. 1998;95(9):5323–5328.

17. Connors BW, Gutnick MJ. Intrinsic firing patterns of diverse neocortical neurons. Trends in Neurosciences. 1990;13(3):99 – 104. doi:http://dx.doi.org/10.1016/0166-2236(90)90185-D.

18. Benda J, Herz AVM. A Universal Model for Spike-Frequency Adaption. Neural Computation. 2003;15(11):2523–2564.

19. Desai NS, Rutherford LC, Turrigiano GG. Plasticity in the intrinsic Excitability of Cortical Pyramidal Neurons. Nature Neuroscience. 1999;2:515–520.

20. Dayan P, Abbott LF. Theoretical Neuroscience. MIT Press; 2001.

21. Hill A. The possible effects of the aggregation of the molecules of haemoglobin on its dissociation curves. The Journal of Physiology. 1910;40:iv—vii. doi:10.1113/jphysiol.1910.sp001389.

22. Philippides A, Husbands P, O'Shea M. Four-Dimensional Neuronal Signaling by Nitric Oxide: A Computational Analysis. Journal of Neuroscience. 2000;20(3):1199–1207.

23. Brette R, Goodman D, Stirnberg M. The Brian spiking neural network simulator (Version 1.0) [Computer Software]; 2016. `http://www.briansimulator.org/`.

24. Team MD. Matplotlib (Version 1.5.3) [Computer Software]; 2016. `https://matplotlib.org/1.5.3/index.html`.

25. Alstott J. powerlaw: A Python Package for Analysis of Heavy-Tailed Distributions (Version 1.4.1) [Computer Software]; 2017. `https://pypi.python.org/pypi/powerlaw`.

26. Azouz R, Gray CM. Dynamic spike threshold reveals a mechanism for synaptic coincidence detection in cortical neurons in vivo. Proceedings of the National Academy of Sciences of the United States of America. 2000;97(14):8110–8115.

27. Jolivet R, Rauch A, Lüscher HR, Gerstner W. Predicting spike timing of neocortical pyramidal neurons by simple threshold models. Journal of Computational Neuroscience. 2006;21(1):35–49. doi:10.1007/s10827-006-7074-5.

28. Loewenstein Y, Yanover U, Rumpel S. Predicting the Dynamics of Network Connectivity in the Neocortex. Journal of Neuroscience. 2015;35(36):12535–12544. doi:10.1523/JNEUROSCI.2917-14.2015.

29. Yasumatsu N, Matsuzaki M, Miyazaki T, Noguchi J, Kasai H. Principles of Long-Term Dynamics of Dendritic Spines. Journal of Neuroscience. 2008;28(50):13592–13608. doi:10.1523/JNEUROSCI.0603-08.2008.

30. Loewenstein Y, Kuras A, Rumpel S. Multiplicative Dynamics Underlie the Emergence of the Log-Normal Distribution of Spine Sizes in the Neocortex In Vivo. Journal of Neuroscience. 2011;31(26):9481–9488. doi:10.1523/JNEUROSCI.6130-10.2011.

31. Hoffmann FZ, Triesch J. Non-random network connectivity comes in pairs. Network Neuroscience. 2017;.

32. Zheng P, Dimitrakakis C, Triesch J. Network Self-Organization Explains the Statistics and Dynamics of Synaptic Connection Strength in Cortex. PLOS Computational Biology. 2013;.

33. Bauke H. Parameter estimation for power-law distributions by maximum likelihood methods. The European Physical Journal B. 2007;58(2):167–173. doi:10.1140/epjb/e2007-00219-y.

34. Clauset A, Rohilla CS, Newman MEJ. Power-Law Distributions in Empirical Data. SIAM Review. 2009;51(4):661–703. doi:10.1137/070710111.

35. Alstott J, Bullmore E, Plenz D. powerlaw: A Python Package for Analysis of Heavy-Tailed Distributions. PLOS ONE. 2014;9(1):1–11. doi:10.1371/journal.pone.0085777.

36. Effenberger F, Jost J. Self-Organization in Balanced State Networks by STDP and Homeostatic Plasticity. PLOS Computational Biology. 2015;.

37. Yassin L, Benedetti BL, Jouhanneau JS, Wen JA, Poulet JF, Barth AL. An Embedded Subnetwork of Highly Active Neurons in the Neocortex. Neuron. 2010;68(6):1043 – 1050. doi:http://dx.doi.org/10.1016/j.neuron.2010.11.029.

38. Eckmann JP, Jacobi S, Marom S, Moses E, Zbinden C. Leader neurons in population bursts of 2D living neural networks. New Journal of Physics. 2008;10. doi:10.1088/1367-2630/10/1/015011.

39. Sjöström PJ, Turrigiano GG. Rate, Timing, and Cooperativity Jointly Determine Cortical Synaptic Plasticity. Neuron. 2001;.

40. Feldman D. The Spike-Timing Dependence of Plasticity. Neuron. 2012;.

41. Couto RT. Green's functions for the wave, Helmholtz and Poisson equations in a two-dimensional boundless domain. Revista Brasileira de Ensino Física. 2013;.

42. Collins CE, Airey DC, Young NA, Leitch JH D B Kaas. Neuron densities vary across and within cortical areas in primates. Proceedings of the National Academy of Sciences of the United States of America. 2010;107.

43. Schüz A, Palm G. Density of neurons and synapses in the cerebral cortex of the mouse. The Journal of Comparative Neurology. 1989;286(4):442–455. doi:10.1002/cne.902860404.

44. Gonçalves JT. Circuit level defects in the developing neocortex of Fragile X mice. Nature Neuroscience. 2013;.

45. Gonçalves JT, O'Donnell C, Sejnowski TJ, Portera-Cailliau C. Two photon calcium imaging recordings of spontaneous activity from mouse somatosensory cortex in wild-type and Fmr1 knock-out mice from three developmental age groups; 2017. Available from: `http://dx.doi.org/10.6080/K0X63K3X`.

46. Allen Institute for Brain Science. Allen Mouse Brain Atlas. Available from: maus.brain-map.org; 2018.

47. Roxin A, Brunel N, Hansel D, Mongillo G, van Vreeswijk C. On the Distribution of Firing Rates in Networks of Cortical Neurons. Journal of Neuroscience. 2011;31(45):16217–16226. doi:10.1523/JNEUROSCI.1677-11.2011.

48. van Vreeswijk C, Sompolinsky H. Chaotic Balanced State in a Model of Cortical Circuits. Neural Computation. 1998;.

49. Koulakov AA, Hromádka T, Zador AM. Correlated Connectivity and the Distribution of Firing Rates in the Neocortex. The Journal of Neuroscience. 2009;.

50. Philippides A, Ott SR, Husbands P, Lovick TA, O'Shea M. Modeling Cooperative Volume Signaling in a Plexus of Nitric Oxide Synthase-Expressing Neurons. Journal of Neuroscience. 2005;25(28):6520–6532. doi:10.1523/JNEUROSCI.1264-05.2005.

51. O'Connor DH, Peron SP, Huber D, Svoboda K. Neural Activity in Barrel Cortex Underlying Vibrissa-Based Object Localization in Mice. Neuron. 2010;67.

52. Vogels TP, Sprekeler H, Zenke F, Clopath C, Gerstner W. Inhibitory Plasticity Balances Excitation and Inhibition in Sensory Pathways and Memory Networks. Science. 2011;334(6062):1569–1573. doi:10.1126/science.1211095.

53. Luz Y, Shamir M. Balancing Feed-Forward Excitation and Inhibition via Hebbian Inhibitory Synaptic Plasticity. PLOS Computational Biology. 2012;8(1):1–12. doi:10.1371/journal.pcbi.1002334.

54. Dragoi G, Harris KD, Buzsáki G. Place Representation within Hippocampal Networks Is Modified by Long-Term Potentiation. Neuron. 2003;39(5):843 – 853. doi:http://dx.doi.org/10.1016/S0896-6273(03)00465-3.

55. Sweeney Y, Clopath C. Emergent spatial synaptic structure from diffusive plasticity. European Journal of Neuroscience. 2017;45(8):1057–1067. doi:10.1111/ejn.13279.

56. Hartmann C, Lazar A, Nessler B, Triesch J. Where's the Noise? Key Features of Spontaneous Activity and Neural Variability Arise through Learning in a Deterministic Network. PLOS Computational Biology. 2016;11(12):1–35. doi:10.1371/journal.pcbi.1004640.

Supporting information

S1 Appendix. We would like to derive a linear relation between mean firing rate and the mean rate of NO synthesis. One could naively replace the sum of Dirac functions in (8) by a continuous inflow $[\text{Ca}^{2+}]_{\text{spike}}r(t)$. This approximation would indeed allow for the correct calculation of a linear relation between mean firing rate and NO production if (9) was a linear homogeneous differential equation. The cubic dependence on Ca^{2+} breaks this simplicity. We note the following in order to derive an approximate description: The target firing rate of 3 Hz and the corresponding mean interspike interval of 0.33...s is large compared to the decay constant of calcium, $\tau_{\text{Ca}^{2+}} = 0.01\,\text{s}$. Consequently, it is very unlikely that one spike event will fall into a region where the calcium concentration, decaying from the instantaneous jump of the previous spike event, is still significantly larger than zero. In fact, calculating the mean concentration

of Ca^{2+} before a new spike event over all neurons and all spike events for $1500\,\mathrm{s}$ resulted in a value of 0.0013. As such, one can justify the approximation of replacing the exact expression of $Ca^{2+^3}(t)$, which is a cubed sum of cut off exponential functions, by a sum of cubed exponentials, because only one term of the sum at a time is significantly larger than zero:

$$
\begin{aligned}
Ca^{2+^3}(t) &= \left[[\mathrm{Ca}^{2+}]_{\mathrm{spike}} \sum_i \theta\left(t - t^i_{\mathrm{spike}}\right) \exp\left(-\left(t - t^i_{\mathrm{spike}}\right)/\tau_{\mathrm{Ca}^{2+}}\right) \right]^3 \\
&\approx [\mathrm{Ca}^{2+}]_{\mathrm{spike}}^{\,3} \sum_i \theta\left(t - t^i_{\mathrm{spike}}\right) \exp\left(-3\left(t - t^i_{\mathrm{spike}}\right)/\tau_{\mathrm{Ca}^{2+}}\right)
\end{aligned}
\tag{35}
$$

with $\theta(x)$ being the Heaviside step function. By the same argument

$$
\frac{Ca^{2+^3}(t)}{Ca^{2+^3}(t)+1} \approx \sum_i \theta\left(t - t^i_{\mathrm{spike}}\right) \frac{\exp\left(-3\left(t - t^i_{\mathrm{spike}}\right)/\tau_{\mathrm{Ca}^{2+}}\right)}{\exp\left(-3\left(t - t^i_{\mathrm{spike}}\right)/\tau_{\mathrm{Ca}^{2+}}\right) + \frac{1}{[\mathrm{Ca}^{2+}]_{\mathrm{spike}}^{\,3}}} \,.
\tag{36}
$$

Therefore, the resulting rate of NO synthesis can be decomposed into a sum of time shifted responses onto a single kernel of calcium concentration as a result of a spike. For a spike at $t_{\mathrm{spike}} = 0$, the solution of (9) can be calculated by

$$
\begin{aligned}
nNOS(t) &= \frac{1}{\tau_{\mathrm{nNOS}}} \int_{-\infty}^{t} dt' \exp(-(t-t')/\tau_{\mathrm{nNOS}})\theta(t') \frac{\exp(-3t'/\tau_{\mathrm{Ca}^{2+}})}{\exp(-3t'/\tau_{\mathrm{Ca}^{2+}}) + \frac{1}{[\mathrm{Ca}^{2+}]_{\mathrm{spike}}^{\,3}}} \\
&= \frac{1}{\tau_{\mathrm{nNOS}}} \int_{0}^{t} dt' \exp(-(t-t')/\tau_{\mathrm{nNOS}}) \frac{\exp(-3t'/\tau_{\mathrm{Ca}^{2+}})}{\exp(-3t'/\tau_{\mathrm{Ca}^{2+}}) + \frac{1}{[\mathrm{Ca}^{2+}]_{\mathrm{spike}}^{\,3}}} \,.
\end{aligned}
\tag{37}
$$

The exact solution of this integral can be expressed in terms of the hyper-geometric function, making it rather impractical for any further analysis. Looking for further simplifications, we noted that τ_{nNOS} is ten-fold larger than $\tau_{\mathrm{Ca}^{2+}}$. This discrepancy in decay times allows for the assumption that the impact of the calcium kernel onto $nNOS$ is practically instantaneous. Consequently, $nNOS(t)$ becomes

$$
nNOS(t) = \frac{1}{\tau_{\mathrm{nNOS}}} \theta(t) \exp(-t/\tau_{\mathrm{nNOS}}) \int_{0}^{\infty} dt' \frac{\exp(-3t'/\tau_{\mathrm{Ca}^{2+}})}{\exp(-3t'/\tau_{\mathrm{Ca}^{2+}}) + \frac{1}{[\mathrm{Ca}^{2+}]_{\mathrm{spike}}^{\,3}}} \,.
\tag{38}
$$

In this form, the integral has an easy-to-handle solution, which — with all spike events now included — results in

$$
nNOS(t) = \frac{[\mathrm{Ca}^{2+}]_{\mathrm{spike}}^{\,3}\,\tau_{\mathrm{Ca}^{2+}}\,\ln(2)}{3\tau_{\mathrm{nNOS}}} \sum_i \theta(t - t^i_{\mathrm{spike}}) \exp(-(t - t^i_{\mathrm{spike}})/\tau_{\mathrm{nNOS}}) \,.
\tag{39}
$$

Fig. 9 compares the approximation given by (39) to the full NO production model (equations (8) and (9)). Spikes were drawn from a Poisson process at a rate of 3 Hz. The simplified model fits very well for sufficiently isolated spike events, as predicted. One can observe a slightly smaller but acceptable agreement for the rare event of two subsequent spikes appearing very close to each other, as seen in Fig. 9 at approximately 4 seconds.

Thus, on average, the sum in (39) simply reduces to the mean rate $\langle r \rangle$:

$$
\langle nNOS \rangle = \frac{[\mathrm{Ca}^{2+}]_{\mathrm{spike}}^{\,3}\,\tau_{\mathrm{Ca}^{2+}}\,\ln(2)}{3\tau_{\mathrm{nNOS}}} \langle r \rangle \,.
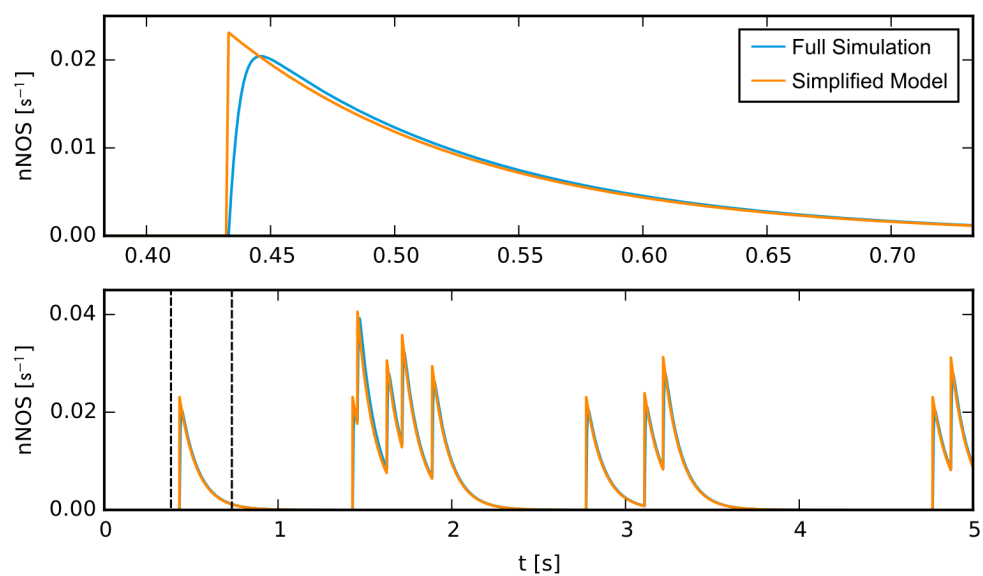\tag{40}
$$

Fig 9. nNOS under Poisson spiking. Time course of nNOS(t) with Poisson spiking at 3 Hz. The full simulation (blue, see equations (8),(9)) is well fitted by the simplified model (orange, see (39)). Top axis is a closeup of the first spike event.